

# A Numerical Study on the Characteristics of the System Propeller and Rudder at Low Speed Operation

Vladimir Krasilnikov<sup>1</sup>, Dmitriy Ponkratov<sup>2</sup> and Pierre Crepier<sup>3</sup>

<sup>1</sup>Norwegian Marine Technology Research Institute (MARINTEK), Trondheim, Norway

<sup>2</sup>Ålesund University College, Ålesund, Norway

<sup>3</sup>ENSIETA (Ecole Nationale Supérieure D'Ingenieurs), Brest, France

## ABSTRACT

The two meshing approaches, both featuring a high degree of automation but using different mesh and interface topologies, are studied in application to propeller-rudder interaction problem at low speed operation. The results obtained with these two approaches and different solution methods for unsteady propeller-rudder interaction are compared and their advantages and limitations are discussed. Numerical predictions are validated against experimental data, in terms of propeller-induced velocity field, propeller and rudder forces, and cavitation extents. The methods are shown to predict adequate results in a practical range of rudder angles.

## Keywords

Propeller, Rudder, RANS, Low-speed operation

## 1 INTRODUCTION

Successfully designed for a given operation condition (design point), a propulsion system including propeller and rudder may show poorer performance in off-design operation if the relevant off-design conditions are not carefully examined during design process. One of the most challenging situations is related to the so-called "low speed operation" when propeller loading is heavy and interaction between the components of propulsor is strong. Typical examples of low speed operation are given by bollard pull, trawling, slow steady backing and crashback conditions. In real sea operation, propeller and rudder perform behind ship hull, and they encounter complex inflow due to hull wake, drift, current and interaction. These are the problems to address when predicting loads on propulsor during dynamic positioning. Ducted propeller represents a more complex case compared to open propeller. For both economy and time reasons, it is not always possible to conduct extensive model tests to study propulsor performance in off-design conditions. Furthermore, the information obtained from model tests is often limited to averaged integral characteristics (forces and moments), and it is obtained in model scale. For a more detailed analysis of interaction effects, CFD methods are to be used.

Concerned with propeller-rudder interaction problem, the CFD methods range, in terms of approach employed, from potential BEM codes (Ghassemi & Allievi 1999, Achkinadze et al 2003), through coupled BEM/Euler (Kinnas et al 2003) and BEM/RANS (Krasilnikov et al 2003, Han et al 2008) solutions, to full viscous simulations by RANS (Lübke 2007, Sánchez-Caja et al 2008, 2009). When choosing a method for practical analyses, the user is normally guided by a combined criterion of "robustness-economy-accuracy-simulation targets". It is understood that the problems we face at low speed operation can only be trust worthily resolved by fully viscous flow methods, and this is the area where most numerical efforts are currently being put into. While in recent years we have witnessed successful application of LES approach to unsteady crashback simulations of open (Chang et al 2008), to ducted propellers (Jang & Mahesh 2008) and to modeling of unsteady propeller cavitation (Bensow et al 2008), RANS method remains the only realistic option for engineers.

Even though RANS simulation of propellers is becoming a routine practice in research institutes, it still may represent a challenge for designers, especially if simulated arrangement contains additional components such as duct and rudder. Both the meshing and the solution techniques require some considerable experience before they can be relied upon in everyday design practice. To facilitate engineering efforts, a number of automated CFD pre-processing tools have been developed for propeller problems. Among those is the pre-processing method described in Krasilnikov et al (2007, 2009) and Krasilnikov & Sun (2008). This method is oriented to the users of CFD products by ANSYS, as it makes use of the program GAMBIT for mesh generation and the program FLUENT for equation solution. Originally applied to the problems of open, ducted and podded propellers, this method has recently been extended to include the cases of open propeller with rudder and ducted propeller with rudder. It is based on use of hybrid meshes. The development of the aforementioned pre-processing method is the ongoing joint activity between MARINTEK and China Ship Scientific Research Center (CSSRC).

These pre-processing tools are customized to certain target problems. They support arbitrary geometries of propeller, duct and rudder, but are limited to the simulation of propulsors separated from ship hull. Mesh generators of some general-purpose commercial CFD packages offer a very high degree of automation at practically arbitrary simulation setup (STAR-CCM+, 2009).

In the present paper, we will consider comparative validation results obtained with a full RANS solution using the aforementioned pre-processing method and polyhedral meshing technique of STAR-CCM+ for the case of open propeller with rudder, focusing on low speed operation conditions. As far as the force and surface pressure predictions are concerned, validation results for open and ducted propellers have already been presented, to a certain extent, in a number of earlier papers (Krasilnikov et al 2007, Krasilnikov & Sun 2008). From the point of view of propeller-rudder interaction, it was, however, important to evaluate the capabilities of the methods in terms of velocity field prediction in propeller slipstream. Therefore, comparisons with velocity field measurements have been performed. Since the measurements had been carried out in the cavitation tunnel, the presence of tunnel walls was accounted for in the polyhedral meshing method. For the case of open propeller with rudder, we will discuss simulation results obtained with different approaches to resolve propeller-rudder interaction – quasi-steady Moving Reference Frame (MRF) method, steady-state approximation by a Mixing Plane (MP) method and fully unsteady Sliding Mesh (SM) method. Prediction of forces acting on propeller and rudder, and cavitation domains on both components will be addressed.

## 2 MESHING APPROACHES

The two alternative meshing approaches have been adopted in the present study. The first approach follows the methodology of pre-processing technique developed for GAMBIT and FLUENT, and it makes use of hybrid meshes. The second approach applied with STAR-CCM+ is based on the application of unstructured polyhedral meshes. Both approaches offer a very high degree of automation and are, therefore, suitable for engineering use. Below we will consider the key features of these two approaches.

### Approach 1 – Hybrid mesh (FLUENT)

A cylindrical computation domain surrounding propeller and rudder is divided into the two sub-domains – Propeller domain and Rudder domain – separated by an internal interface, as shown in Figure 1. As this approach is intended for the simulation of propeller-rudder arrangements in open water (i.e., separated from any other bodies), it is possible to rotate the whole Propeller domain in the solution. Each of the two aforementioned domains is divided into a number of blocks. There are 6 blocks in the Propeller domain.

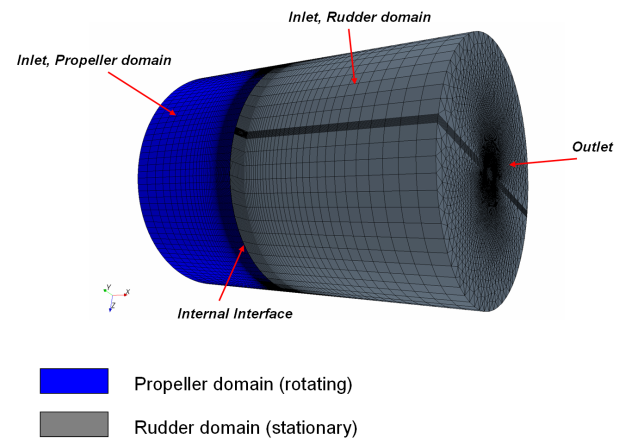


Figure 1: Sub-division of computation domain in the Approach 1.

In the cylindrical block surrounding propeller and hub, an unstructured mesh of tetrahedral cells is built. Mesh generation in this block begins with triangulation of propeller and hub surfaces by the elements with target edge size equal to  $k_{MFP} \cdot 0.005 \cdot D$ , where  $D$  is the propeller diameter, and  $k_{MFP}$  is the mesh factor to regulate mesh fineness. This surface mesh can be uniform or refined towards the blade edges, blade root and tip, and hub ends. Layers of prismatic cells can be grown from the blade and hub surfaces, in order to provide a better resolution of boundary layer flows. This is an optional feature in the mesh generator, and it was not used in the simulations done in the present paper with the Approach 1. Tetrahedral mesh is built in the propeller block using the volume size function which creates cells whose size increases gradually outwards reaching  $3 \cdot k_{MFP} \cdot 0.005 \cdot D$  at the outer boundaries of propeller block. In the cylindrical blocks upstream and downstream of propeller block, which have the same radius as propeller block, prismatic meshes are generated using the Cooper tool. In the outer blocks, hexahedral meshes are used. The meshing of the Propeller domain is, thus, similar to that used in the simulation of propeller without rudder and described in Krasilnikov & Sun (2008) and in Krasilnikov et al (2009). The difference is that downstream of propeller, the domain is only extended to the interface separating Propeller domain and Rudder domain. The interface between the Propeller domain and Rudder domain is located downstream of the hub, at 0.25 of the distance between the aft end of the hub and rudder leading edge at rudder angle zero. In the Rudder domain, a block surrounding rudder and having vertical size equal to rudder span is created. In this block, which is aligned with rudder, according to rudder angle, a structured mesh consisting of 15 layers of hexahedral cells is generated with cell condensation towards the rudder surface. Immediately above and below the rudder, attached to the rudder tips, the two blocks of prismatic cells are created. The volume meshes in the rudder block

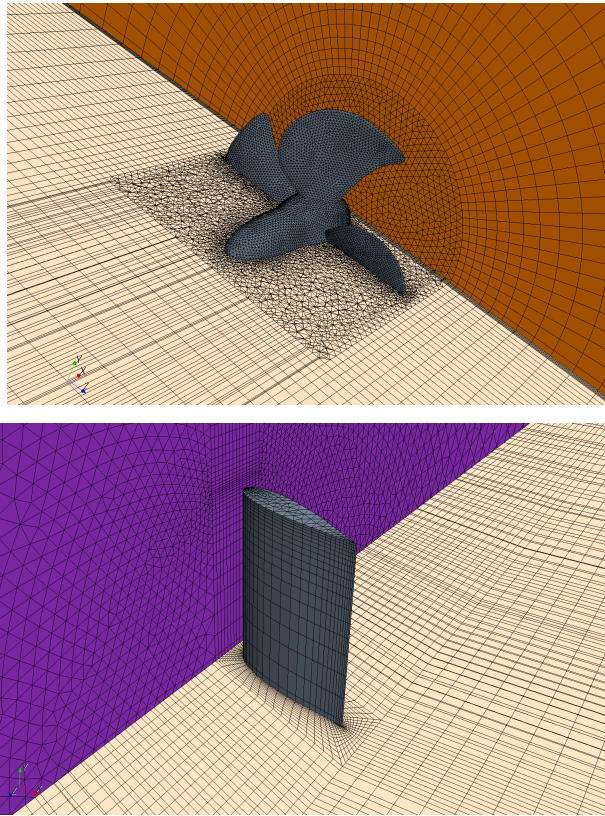


Figure 2: Details of meshes in the Propeller domain and Rudder domain used in the Approach 1.

and the two tip blocks are generated from rectangular surface mesh on the rudder blade and triangular surface meshes on the rudder tips, both featuring condensation towards rudder leading and trailing edges, and towards rudder tips. In the block downstream of rudder (rudder wake), a hexahedral mesh is built, while in the remaining outer blocks the meshes are prismatic. The mesh fineness in the Rudder domain is also regulated by a single mesh factor –  $k_{MFR}$ . Thus, only with two mesh factors supplied, the user can generate mesh in the whole computation domain. The default values of these mesh factors are suggested based on systematic calculations. For model scale simulations, it is recommended to use  $k_{MFP} = 2.0$  and  $k_{MFR} = 2.0$ . For full scale simulation, recommended values of the mesh factors lie in the range from 0.5 to 1.0. These values of the mesh factors will result in coarse near-wall modeling on propeller (without using prismatic mesh layers) and rudder to meet the values of wall  $y^+$  in the range from 30 to 200. Some details of the meshes in the Propeller domain and Rudder domain are illustrated in Figure 2.

#### Approach 2 – Unstructured polyhedral mesh (STAR-CCM+)

An alternative approach implemented in the present study employs fully unstructured polyhedral meshes. It can be used for the simulation of propeller-rudder systems as in open water as in presence of ship hull. The experimental data used for comparisons in this paper were from the

model tests in the cavitation tunnel. Therefore, the numerical model in the Approach 2 included tunnel walls as a cylinder of the radius equal to the radius of tunnel working section, and part of the headbox (referred below as “headbox”) above the rudder that houses rudder axel, as shown in Figure 3. The rotating Propeller domain is represented by one cylindrical propeller block, which corresponds to that of the tetrahedral propeller block in the Approach 1. This block has three internal interfaces (inlet, outlet and circumferential) with the surrounding domain of stationary fluid. The locations of these interfaces are as follows: Inlet –  $0.55D$  upstream of propeller plane; Circumferential -  $0.55D$  from propeller shaft axis; Outlet -  $0.22575D$  downstream of propeller plane, which corresponds to  $0.25$  of the distance between the aft end of the hub and rudder leading edge at rudder angle zero, as in the Approach 1. In the present simulations, the target size of surface mesh triangles on propeller and hub was  $0.01D$ , which corresponded to the mesh factor  $k_{MFP} = 2.0$  in the Approach 1. However, lower values of the minimum surface size ( $0.005D$ ) were allowed, in order to refine the mesh

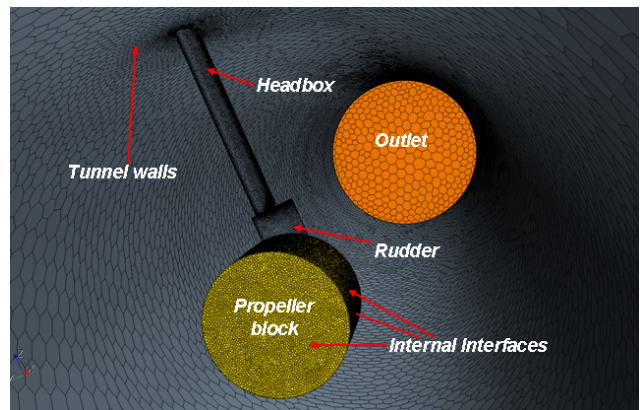


Figure 3: Elements of computation domain in the Approach 2.

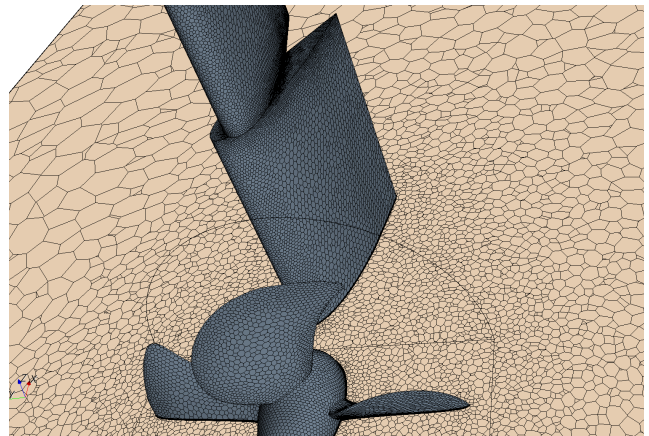


Figure 4: Surface mesh on propeller, rudder and headbox. Plane section of the volume mesh. Approach 2.

towards blade edges, tip and root. The surface mesh size at the interface boundaries was  $0.02D$ . The target surface mesh size on the rudder followed the same settings as that on propeller blades, except for the upper rudder tip where even higher mesh refinement (target  $0.005D$ , minimum  $0.0025D$ ) was required in order to ensure appropriate resolution of the flow in the gap between the rudder and headbox. Prismatic meshes having total relative thickness  $0.005D$  and including 10 cell layers with the stretching factor of 1.1 were extruded around propeller blades, hub, rudder and headbox. Inside the gap between the rudder upper tip and headbox, the thickness of prismatic cell layers was reduced to  $0.0025D$ . Prismatic cell layers were also placed along the tunnel wall boundary. The mesh used in the Approach 2 is intended for an enhanced (all  $y^+$ ) wall treatment that emulates performance of the wall function approach where the mesh resolution is coarser and performance of fine near-wall resolution where the mesh is fine enough to resolve viscous sub-layer, providing, at the same time, smooth blending across the buffer layer. For a typical simulation, the aforementioned settings yield the following values of wall  $y^+$ : Tunnel walls -  $0 \div 3$ , Headbox -  $0 \div 5$  (up to 11, in local patches adjacent to the gap); Rudder -  $0 \div 11$  (up to 22, in local patches adjacent to the gap and near rudder leading edge, where the rudder surface encounters trailing vortices of propeller wake); Propeller blades and hub -  $0 \div 11$  (up to 25, in the areas near blade tip and trailing edge). It is, of course, possible to achieve a higher degree of near-wall resolution everywhere by further refinement of the mesh.

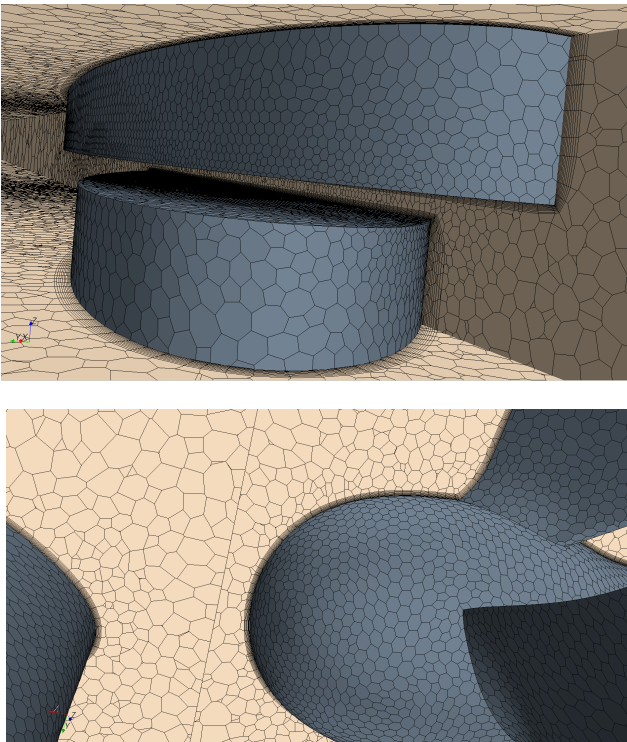


Figure 5: Details of polyhedral mesh with prismatic cell layers around propeller, rudder and headbox.

However, as the test calculations have shown, this brings only marginal differences in integral forces and pressure distributions – the quantities that have been in the primary focus of the present study. At the same time, it appears nearly impossible to avoid local zones of higher  $y^+$  values altogether in the domains of separation, vorticity shedding and vortex-surface impingement.

### 3 SOLUTION STRATEGIES

The system of the RANS equations for mass and momentum transfer is closed up with the SST  $k-\omega$  turbulence model. The reasons for the choice of this turbulence model are explained in Krasilnikov & Sun (2008) and Krasilnikov et al (2009). The transport equations of the problem are solved by a segregated solution method with a SIMPLE-type algorithm for pressure-velocity coupling. The spatial discretization of convection terms is achieved by a second-order upwind scheme which is applied to both the momentum and turbulence transport properties. The diffusion terms are central-differenced and they are second-order accurate. The numerical solution is done by an aggregative algebraic multi-grid (AAMG) solver that is based on a Gauss-Seidel type of iteration technique. A fixed F-cycle method for pressure and a flexible cycle method for momentum are chosen for multi-grid cycling procedure. The values of under-relaxation factors are set somewhat lower than default values, specifically: for pressure – 0.3, for momentum – 0.5; for turbulent kinetic energy and specific dissipation rate – 0.5; for turbulent viscosity – 1.0. All the above settings have been kept identical in both the Approach 1 and the Approach 2.

A separate issue is related to resolving unsteady interaction between the rotating propeller and stationary rudder. As the earlier studies have demonstrated, propeller-rudder interaction can, in principal, be resolved using different solution methods such as Moving Reference Frame (MRF), Mixing Plane (MP) and Sliding Mesh (SM) (Sánchez-Caja et al 2009). Of these methods, only time-accurate SM method provides a completely strict solution to the problem on hands, but it is also most expensive. The quasi-steady MRF method and steady MP method can only be considered as approximations of the exact time-accurate solution. Depending on simulation targets, these approximations may suffice objective of the study to a larger or lesser extent. Simplified methods are shown to accurately predict the integral forces on propeller and rudder, but they are not representative as far as the amplitudes of fluctuating forces are concerned. Besides, MRF and MP approaches reveal sensitivity to the position of the downstream interface between the rotating and stationary mesh blocks (Sánchez-Caja et al 2009). As a general rule, the simplified methods offer higher accuracy when the interaction between the rotating and stationary domains is weak, which is, definitely, not the case at low speed operation when propeller loading is heavy and propeller induces high velocities in the slipstream.

All the three aforementioned methods were exploited in the present study. In the MRF simulation, only one position of propeller with its key blade at top vertical position (0 degrees) was considered. It was not the objective to perform a truly quasi-steady analysis by running calculations at several fixed positions of propeller. We only aimed at comparing the levels of forces obtained from different solution approaches. Such a comparison is justified by the fact that in the propeller-rudder interaction problem, the amplitudes of unsteady propeller and rudder forces are small. The MP simulation represents a steady state approximation of the solution as the rotating and stationary domains exchange by the profiles of circumferentially averaged fluxes through their common interfaces. The MP method was used only with the meshing Approach 1 with a single interface extended across the whole computation domain. On the downstream boundary of Propeller domain, a “pressure outlet” boundary condition was imposed; while on the upstream boundary of Rudder domain, a “pressure inlet” boundary condition was used. Conservation of swirl was enforced at the MP interface.

The unsteady SM simulations were carried out using an implicit first-order temporal discretization scheme. The time step corresponded to propeller turn to 1 degree. In the course of preliminary studies, it was found that simulation results reveal certain sensitivity to the time step even in the case of propeller without rudder. Therefore, in order to ensure consistent and accurate time-dependent solution, it was decided to keep the time step sufficiently small. The simulation time depended on case specific conditions and, first of all, on propeller and rudder loading. So, for lower advance coefficients and higher rudder angles, a longer simulation time was required in order to achieve converged periodic pattern. With the Approach 2, comparisons were performed between the time-dependent simulations starting from different initial conditions – fully converged results of a MRF simulation, in one case, and from “start-up” condition, in another case. The final results of these two simulations appear to be very close. However, simulation according to the former method allowed for somewhat faster convergence. For example, in the case of  $J = 0.4$  and rudder angle  $\delta_R = -20^\circ$ , a periodic pattern of propeller and rudder forces in the simulation starting with MRF results was established already after two complete propeller revolutions. In the simulation beginning with “start-up” initial condition, four complete propeller revolutions were required in order to reach converged behavior of rudder axial and side forces. The propeller forces showed faster convergence than rudder forces.

An interesting study done in Sánchez-Caja et al (2008) suggests that location of downstream interface between rotating and stationary domains may have influence on computation results with MRF and MP method due to so-called “numerical blockage”. It is concluded that in order to minimize “numerical blockage”, the downstream interface should preferably be placed further upstream

from rudder to maintain weak interaction between domains separated by the interface. On the other hand, as the tests done in the present study have demonstrated, it is also undesired to place an interface too close to rotating propeller blades. Apparently, due to the interpolation of fluxes across the interface, disturbances in the flow may occur, and they can be seen in the velocity field in propeller slipstream. In particular, such disturbances are evident, if the mesh topologies on the opposite sides of an interface are different, as in the Approach 1. These disturbances vanish when the interface is moved further downstream from the blade. This is, presumably, due to the fact that vortex sheets leaving the blades have sufficient space to progress before encountering interface. In the present work, a compromised location of the downstream interface was therefore chosen as  $0.25$  of the distance between the downstream end of propeller hub and rudder leading edge at rudder angle zero. This location was used in the simulations with all solution methods and with both the Approach 1 and Approach 2.

#### 4 COMPARISONS

In the course of validation studies, comparisons were made between the two approaches and different solutions methods for propeller-rudder interaction. Numerical results were compared with available experimental data. These comparisons included prediction of velocity field in the slipstream of propeller without rudder, integral characteristics of propeller and rudder and cavitation domains on propeller blades and rudder. As mentioned in Section 2, the experimental data were obtained from the model tests done in the cavitation tunnel, which limited the lowest advance coefficient by the value of 0.4. In order to evaluate possible effect of tunnel walls and presence of the headbox housing rudder axel, their geometries were modeled in the Approach 2. The diameter of circular working section of the tunnel was 0.8m. The propeller model had diameter of 0.25m, and it was tested at 16Hz. A desired  $J$  value was achieved by adjustment of water speed.

The geometrical details of propeller and rudder are reduced in Table 1.

##### 4.1 Velocity field in propeller slipstream

The location of the measurement plane in the velocity field measurements without rudder corresponded to the location of rudder axis, i.e.,  $0.5D$  downstream of propeller plane. The comparisons made for the advance coefficient  $J = 0.4$  are presented in Figures 6 and 7 as circumferential averaged distributions of the axial and tangential propeller-induced velocity components. It can be concluded that numerical results according to the Approach 1 and the Approach 2 are in close agreement. No non-physical behaviors were observed in the velocity distributions indicating that fluxes were adequately

Table 1: Geometrical details of propeller and rudder.

<b>Propeller</b>	
Hub/Diameter ratio, $d_H/D$	0.25
Number of blade, $Z$	4
Blade area ratio, $A_B/A_0$	0.62
Pitch setting, $P_{0.7}/D$	1.095
Sections	NACA66mod
Direction of rotation	Right-handed
<b>Rudder</b>	
Height, $L/D$	1.251
Height/chord ratio, $L/c$	1.9156
Section thickness, $t_0/c$	0.2068
Sections	NACA00xx
Distance between propeller plane and rudder axis, $X_R/D$	0.5
Distance of rudder axis from leading edge, $x_{R,A}/c$	0.288

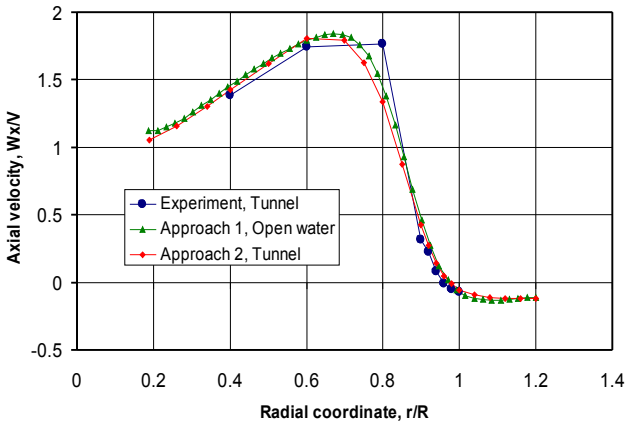


Figure 6: Axial velocity in propeller slipstream.

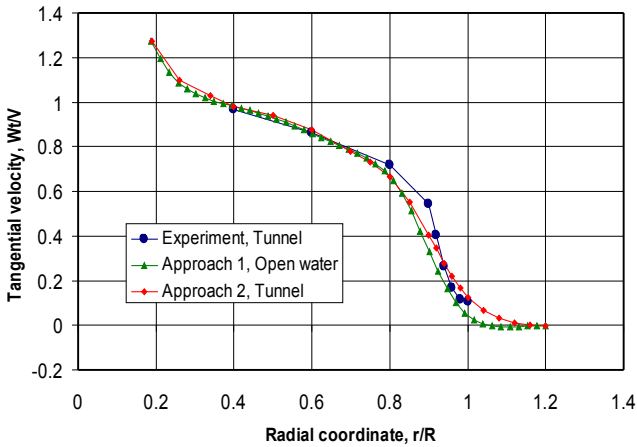


Figure 7: Tangential velocity in propeller slipstream.

transferred through the downstream interface. One can also notice that predicted slipstream contraction meets that measured in the tests. There was no evidence of strong effect of tunnel walls in the simulations. However, at the outer radial locations in the slipstream, the results for tangential velocity obtained with the Approach 2 (where tunnel walls had been included) were somewhat closer to the measured data. The numerical and experimental values of propeller thrust and torque at the point of comparison are presented in Table 2.

Table 2: Calculated and measured thrust and torque coefficients of propeller without rudder at  $J = 0.4$ .

	$K_T$	$K_Q$
Experiment	0.387	0.0619
Calc., Approach 1	0.38508	0.06186
Calc., Approach 2	0.38311	0.06155

A good agreement between the calculated and measured propeller characteristics shows that induced velocities above were compared at the same loading of propeller. A slight under-prediction of propeller forces might be caused by the fact that numerical analyses were done under assumption of fully turbulent flow, while in the tests the zones of laminar flow could be present on propeller blades. The existence of such zones is far not unusual in model tests of propellers where no special measures are taken for artificial flow turbulization. The thrust and torque coefficients according to the Approach 2 are slightly lower than the values obtained by the Approach 1, because of the larger effect of frictional forces in blade boundary layer on section lift. This is the result of a more detailed resolution of boundary layer with a finer mesh of prismatic cell layers used in the Approach 2.

#### 4.2 Integral characteristics of propeller and rudder

We will begin our presentation of validation results concerning propeller and rudder forces with a more detailed comparison between the different meshing approaches and solution strategies for one selected condition –  $J = 0.4$ ,  $\delta_R = -20^\circ$ . The rudder angle  $\delta_R$  is considered positive when rudder trailing edge is turned to starboard. The sign convention for rudder angle and forces is explained in Figure 8. The numerical predictions of propeller and rudder forces obtained by the Approach 1 and Approach 2 are presented in the table included in the Appendix A1. Simulations according to the Approach 1 corresponded to propeller and rudder in unbounded flow. They were performed using the three different methods for propeller-rudder interaction: MRF with key blade of propeller blade fixed at top position; MP with swirl conservation; and MRF+SM where time-accurate solution was done starting with the initial conditions given by MRF results.

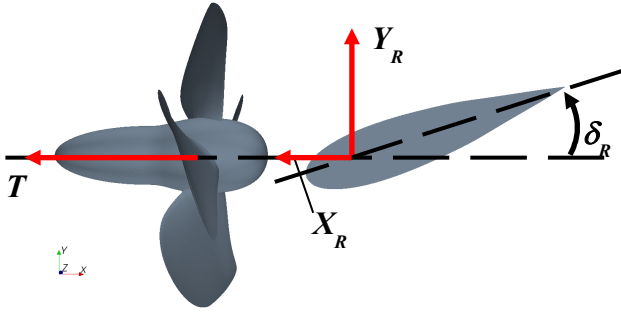


Figure 8: Sign convention for rudder angle and forces.

The Approach 2 included the effects of tunnel walls and headbox, as in the tests. Simulations according to the Approach 2 were done with MRF+SM method as above and pure SM method launched from “start-up” condition. Since in the tests there was no boundary plate installed above the rudder, flow around the headbox and in the gap between the headbox and rudder could have influence on the measurements of rudder forces. Forces acting on the headbox were also computed separately.

Comparison of the results from the Approach 1 obtained with different solution methods for propeller-rudder interaction shows only small differences in propeller thrust and torque. Propeller thrust is slightly higher, while propeller torque is slightly lower in both the MRF and MP predictions, compared to unsteady time-accurate SM results. One should not be misled by the fact that MRF and MP predictions of propeller thrust appear somewhat closer to the measured data. As it has been shown above, for the single propeller, numerical predictions of  $K_T$  are lower than the measured value, and similar tendency could be expected in the propeller-rudder case too. Therefore, the results of time-accurate calculation appear logical. The rudder forces reveal larger differences between the solution methods. Both the MRF and MP methods over-predict rudder axial force and under-predict rudder side force compared to the time-accurate SM results. Concerning the MRF predictions, it should be remembered that they are obtained only for one fixed position of propeller with respect to rudder. Calculations and following averaging of the results for different positions of propeller would bring such quasi-steady approximation closer to the time-accurate SM solution. At the same time, the results obtained with the MP method give us an indication of inaccuracies that arise due to flow averaging at the mixing plane interface. It has to be mentioned that the agreement between the MP and SM results depends on loading conditions and on the magnitude of rudder angle. At lighter loadings and smaller rudder angles the agreement is closer, while at heavier loading and larger rudder angles the agreement is poorer. These trends have also been observed in more recent simulations of a ducted propeller with rudder done by the authors. Clearly, the accuracy of MP approximation is higher when the interaction between the rotating and

stationary domains is weaker. At very heavy loadings of propeller (e.g., low  $J$ ) convergence issues arise in MP simulation.

Comparing numerical predictions performed by the Approach 1 and the Approach 2 using time-accurate SM method one can notice a very close agreement in terms of propeller thrust, propeller torque and rudder axial force. Such an agreement between simulations done with quite different meshing techniques and with different solvers gives one confidence in numerical results obtained. The difference in rudder side force prediction was, however, about 7.5%. This is primarily related to different degrees of near wall resolution achieved with the Approach 1 and the Approach 2, which is manifest in pressure distribution on the suction side of the rudder in the upper part of propeller slipstream. This part of rudder gives the main contribution to the side force. As one can see from the comparison of pressure distributions presented in Figure 9, the Approach 2 featuring fine near-wall resolution, due to denser mesh and prismatic cell layers around rudder surface, predicts lower pressure in the area stretching from rudder leading edge to rudder axis. For the same reason, the Approach 2 predicts higher friction too, but its contribution into the side force is minor compared to the pressure component.

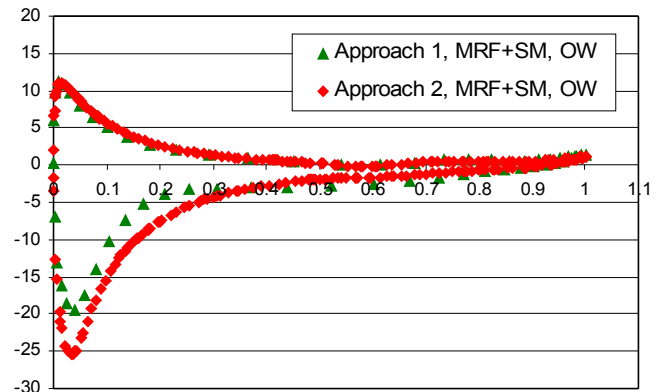


Figure 9: Distribution of pressure coefficient along the rudder section  $z = 0.7R$ . Top key blade position.

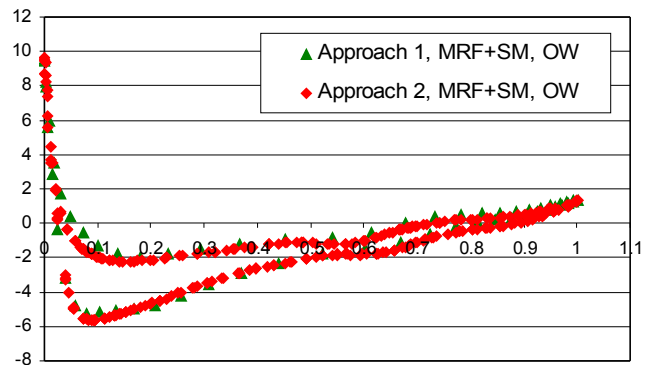


Figure 10: Distribution of pressure coefficient along the rudder section  $z = -0.7R$ . Top key blade position.

At the same time, pressure predictions on the pressure side of the rudder (Figure 9) and on both sides of the rudder in the lower part of propeller slipstream (Figure 10) are very close. The results by the Approach 2 presented in Figures 9 and 10 were obtained from an additional simulation in open water conditions in order to exclude possible effects of tunnel walls and headbox. The differences in prediction of rudder side force between the Approach 1 and Approach 2 become smaller with decreasing magnitude of rudder angle, when the peak of low pressure on the suction side of the rudder is less pronounced. It can also be concluded from the comparisons that the results of time-accurate SM calculations show little dependence on initial conditions. Unsteady SM simulations beginning with converged MRF results converged faster than pure SM simulations beginning with “start-up” condition.

In terms of propeller thrust and torque and rudder axial force, the numerical predictions are found to be in good agreement with the measurements. As to the rudder side force, it can be noticed that numerical results by both approaches are below the values measured in the tests. Adding the side force computed on the headbox to the side force on the rudder brings the total value very close to the measured data. This can indicate that, in the tests, the measurements were affected by the presence of the headbox and, furthermore, the contribution of the headbox was, actually, measured. The contribution of the headbox into the total axial force is insignificant, but in the side force it appears to be at the level of 12%. Visualization of velocity vectors around the lower part of the headbox presented in Figure 11 shows that the inflow comes on the headbox at certain angle, which results in reduced pressure on the starboard (suction) side and increased pressure on the port (pressure) side of the headbox. This asymmetry is due to the redistribution of velocity field caused by both the rotation of the flow induced by propeller and deviation of the flow caused by rudder, in a confined space of cavitation tunnel.

The complexity of interaction taking place between the propeller, rudder and headbox is illustrated by the same Figure 11, where velocity vectors on the approach to the portside of the rudder and headbox are visualized along with pressure distribution on the aforementioned surfaces. It can be seen that due to the blockage of the swirled propeller slipstream by rudder, the velocity vectors are deviated upwards on the pressure side of the rudder. This explains commonly observed phenomenon that cavitating blade tip vortex from propeller migrates upwards after encountering rudder surface. The areas of reduced pressure on the portside of the rudder around the gap between rudder tip and headbox indicate domain where the flux accelerated in the gap is ejected in ambient flow. The flow acceleration in the gap poses potential risk of gap cavitation.

We will now return to the analysis of force prediction and consider the results obtained for other rudder angles

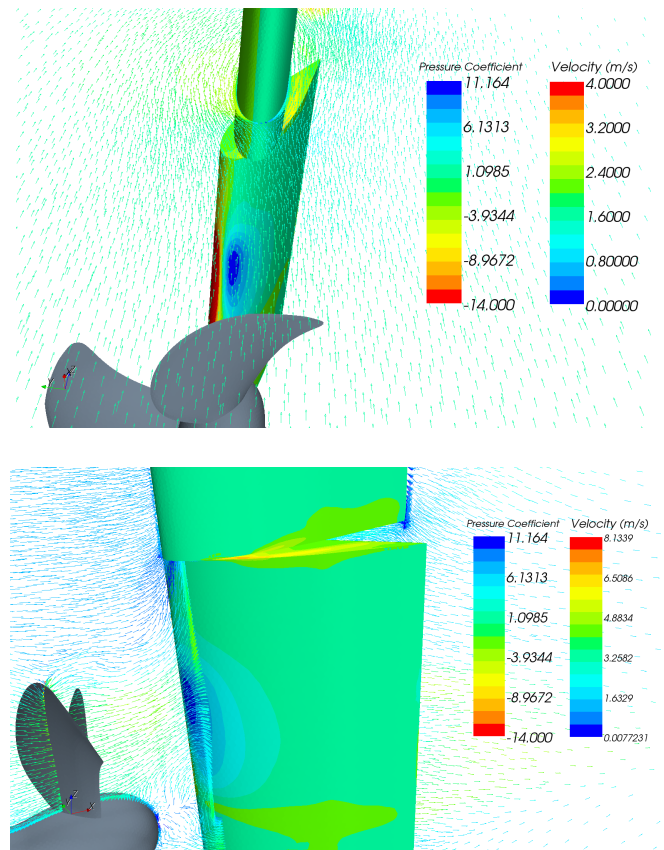


Figure 11: Pressure distribution on the rudder and headbox. Velocity vectors in the ambient flow.

against respective experimental data. Only calculations according to the Approach 2 including tunnel walls and headbox will be presented.

Firstly, we will address the effect of rudder on propeller thrust and torque. The results are presented as absolute figures and as relative values in Figures 12 and 13. The numerical predictions confirm increase of propeller characteristics due to blockage of the slipstream by rudder, as registered in the tests. Both the thrust and torque of propeller become larger with increasing rudder angle, as the rudder blocks a greater part of the slipstream. Simulations show somewhat more symmetric variation of thrust, and they over-predict the increase of torque compared to the test data. However, the maximum difference between the numerical results and experimental values is only 2% in propeller thrust and 2.4% in propeller torque.

The analysis of calculation results shows that blockage of propeller slipstream by rudder results not only in increase of thrust produced by the blades, but also in change of hub contribution into the total thrust. For example, in the considered case of  $J = 0.4$  without rudder, hub gave negative contribution of  $-0.6\%$  of total thrust. With rudder installed at  $\delta_R = -20^\circ$  behind propeller, the hub produced positive thrust of the magnitude of  $+0.85\%$  of total thrust.

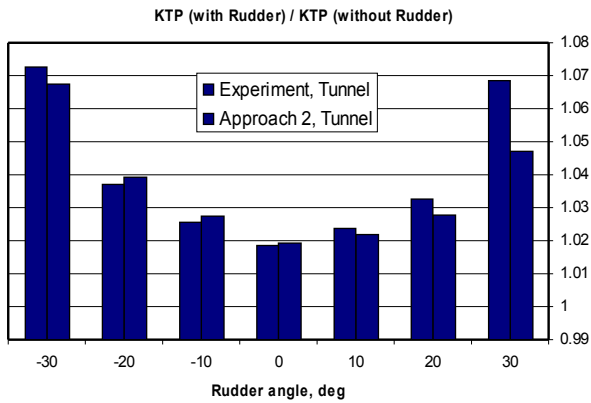
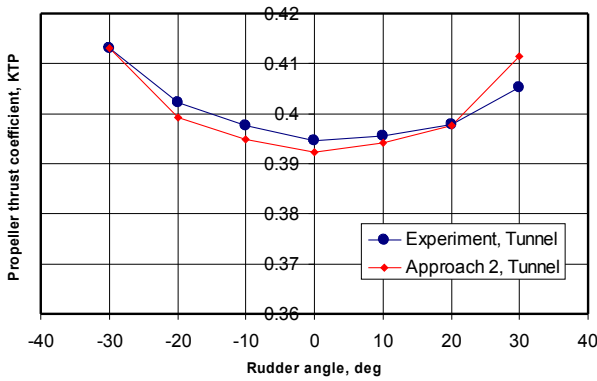


Figure 12: Comparison between the calculated and measured propeller thrust at different rudder angles.

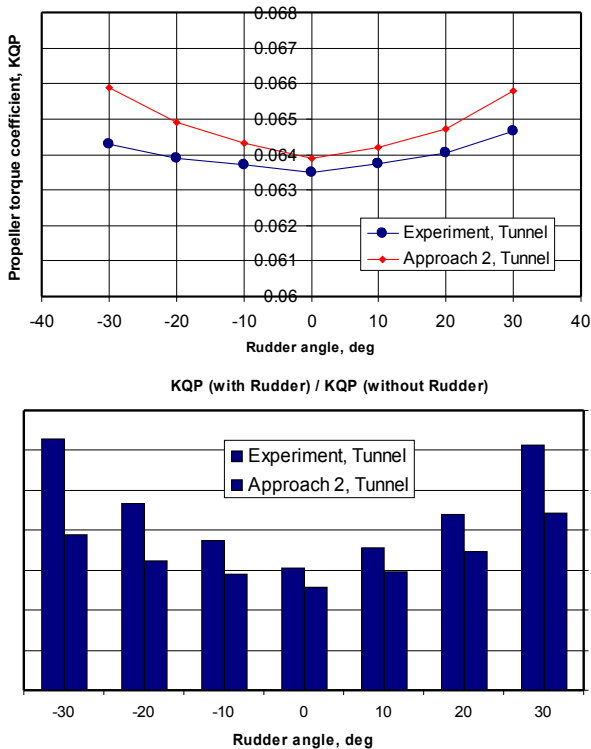


Figure 13: Comparison between the calculated and measured propeller torque at different rudder angles.

The change of hub contribution is caused by re-distribution of pressure on the downstream end of the hub

and on the blade roots. The pressure distributions on propeller blades and hub without and with rudder are illustrated in Figure 14. It can be seen that due to the influence of rudder, the domains of higher pressure appear extended on the pressure side of the blades. The pressure is also increased on the downstream part of the hub. The presence of rudder introduces asymmetry in pressure distributions on the aforementioned surfaces and shifts the location of the detachment of the hub vortex.

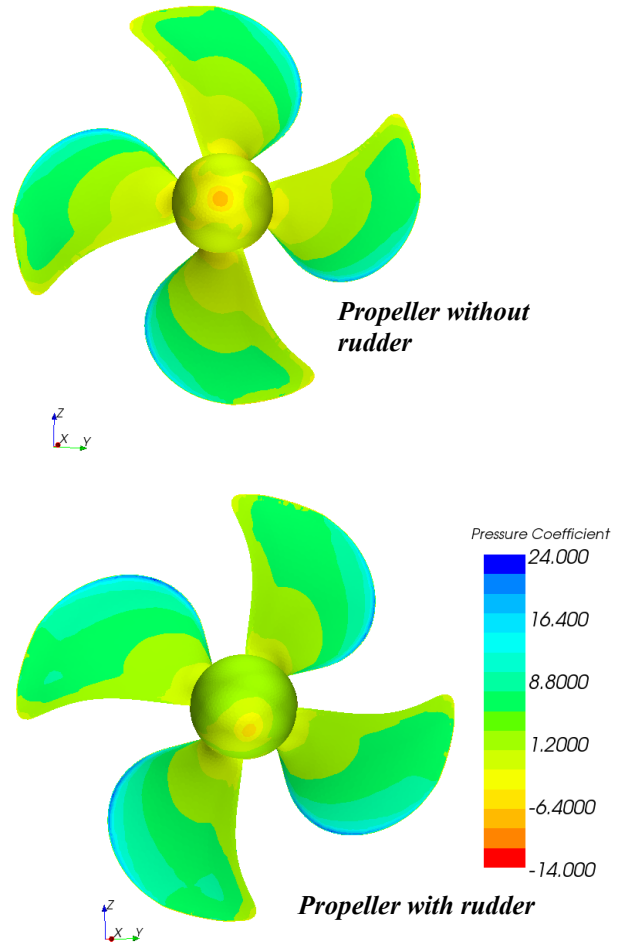


Figure 14: Pressure distribution on propeller blades and hub without rudder and with rudder installed at  $\delta_R = -20^\circ$ ,  $J = 0.4$ .

A comparison between the calculated and measured rudder forces is illustrated in Figure 15, for the axial force, and in Figure 16, for the side force. It prompts an optimistic conclusion that in the range of rudder angles from minus to plus  $20^\circ$ , the applied method allows for sufficiently high accuracy. The discrepancies are noticed at larger rudder angles, such as  $-30^\circ$  and  $+30^\circ$ . The analysis of flow field around the rudder revealed that at such large rudder angles, intensive separation was predicted on the suction side of the rudder. Highly unsteady pattern of cavitation observed in the tests with the present rudder at the rudder angles  $-30^\circ$  and  $+30^\circ$  suggested that separation had taken place under these conditions, but, apparently, in the numerical analyses its

extent had been exaggerated because of the limitations of isotropic turbulence model.

### 4.3 Cavitation on propeller and rudder

Finally, we will consider prediction of cavitation on propeller blades and rudder. In the tests, cavitation was observed at the following conditions:  $J = 0.4$ ,  $\sigma_0^{(V)} = 13.227$ , where cavitation number  $\sigma_0^{(V)}$  was based on the speed of oncoming flow. In order to predict cavitation numerically, simulation of the state change in a two-phase flow mixture should be performed with an appropriate cavitation model to describe the rates of vapor generation and condensation. Such a modeling was beyond the scope of the present study. Instead, in a single-phase simulation, the volumes of cavitation were simply defined as thresholds of pressure coefficient  $-C_p < \sigma_0^{(V)}$  in the fluid volume. This simplified method allows one to identify the zones of cavitation inception and get a first approximation of the extent of cavitation volumes.

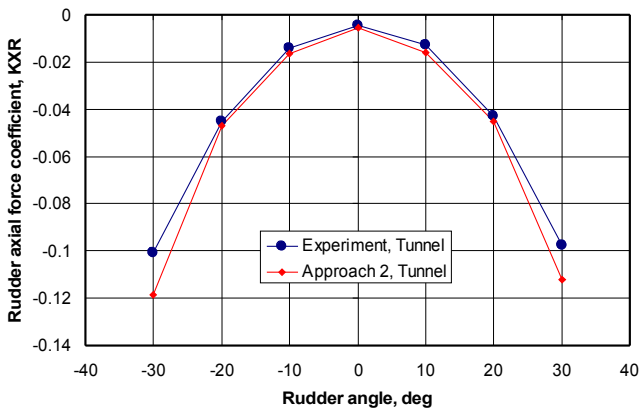


Figure 15: Comparison between the calculated and measured rudder axial force at different rudder angles.

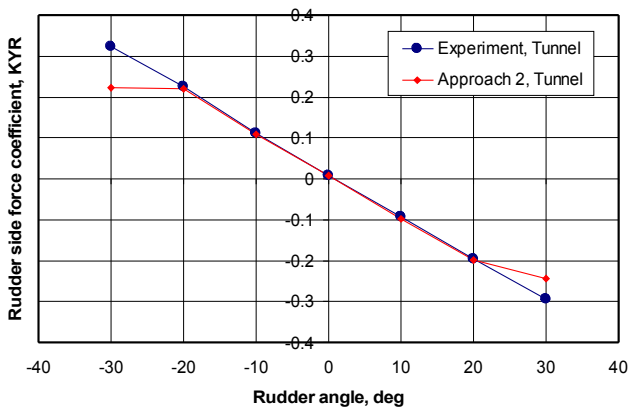


Figure 16: Comparison between the calculated and measured rudder side force at different rudder angles.

Computations were done according to the Approach 2. In the tests, under the specified conditions, cavitation was observed on propeller blades in the form of leading edge sheet cavitation beginning at the radius  $0.5R$ . Cavity thickness increased towards the blade tip where leading edge sheet cavitation merged with cavitating tip vortex.

Threshold diagrams of blade cavitation presented in Figures 17 and 18 reflect the tendencies observed in the tests. More specifically, it is seen that cavities occur from the same radial location as in the tests, and cavity thickness and volume grow towards blade tip. The cavitation in the tip vortex in propeller slipstream is, however, not resolved, which is a consequence of both insufficient mesh resolution and adopted turbulence model. The size of cavities on propeller blades varies somewhat depending on blade position with respect to rudder. However, this variation is quite small. Cavitation on the rudder surface was observed on the suction side of the rudder at the magnitudes of rudder angle larger than  $15^\circ$ , for both the starboard and portside rudder turns. Comparison between the numerical predictions and experimental observations is illustrated in Figures 17 and 18 for the rudder angles  $-20^\circ$  and  $+20^\circ$ , respectively. The location of cavitation domains is predicted correctly by the numerical method.

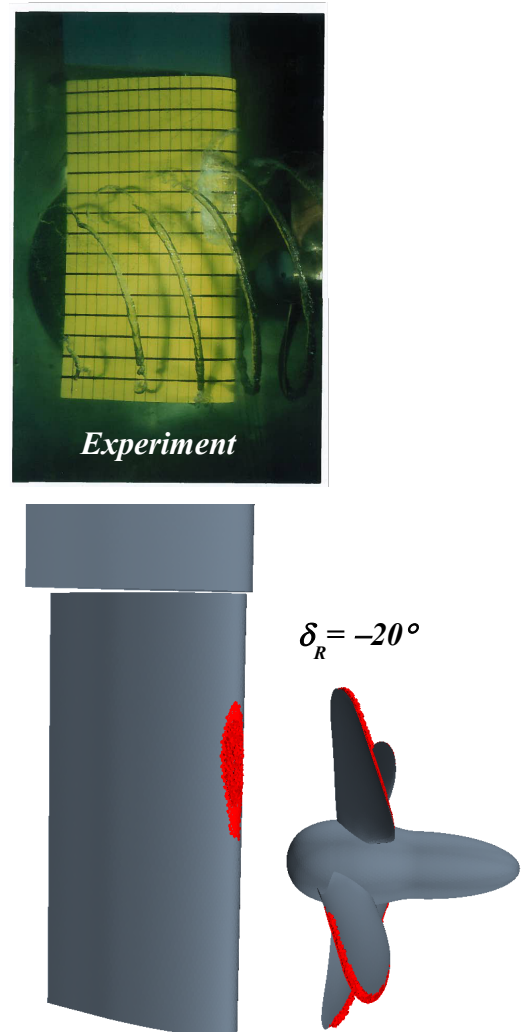


Figure 17: Cavitation on rudder at  $J = 0.4$ ,  $\sigma_0^{(V)} = 13.227$  visualized as a volumetric threshold of pressure coefficient. Rudder angle  $\delta_R = -20^\circ$ .

Cavitation extent on the starboard side is predicted close to the experimental observations. On the portside, it appears over-predicted. It should be noticed that due to the periodic nature of the flow, rudder cavitation is an unsteady process. Unsteadiness of cavities is also influenced by dynamic processes of cavity detachment and closure, as well as an impingement of vortices from propeller. Numerical results presented in Figures 17 and 18 correspond to the position of the key propeller blade around  $0^\circ$  (top position). From the tests, only instantaneous photos of cavitation were available, and it was not always possible to tell to exactly what blade positions they were referred.

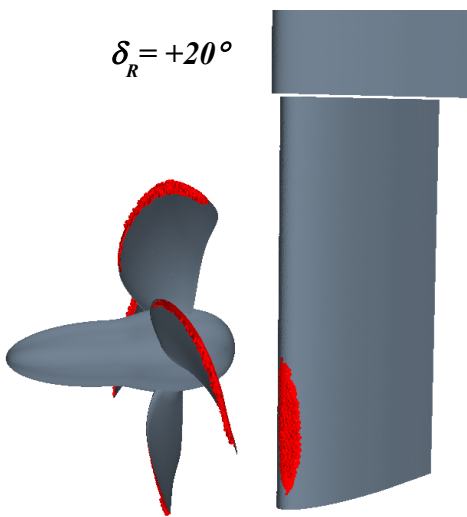
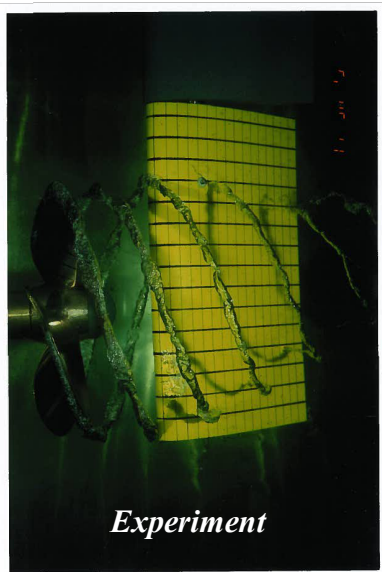


Figure 18: Cavitation on rudder at  $J = 0.4$ ,  $\sigma_0^{(f)} = 13.227$  visualized as a volumetric threshold of pressure coefficient. Rudder angle  $\delta_R = +20^\circ$ .

## 8 CONCLUSIONS

The two meshing approaches, both featuring a high degree of automation, but using different mesh and interface topologies have been applied, in the present work, to the RANS modeling of propeller-rudder interaction. The

approaches are shown to offer comparable accuracy in terms of propeller induced velocity field, propeller and rudder forces and rudder surface pressure distribution. Time-accurate simulation with a Sliding Mesh method brings results that are in close agreement with experimental data, in terms of all integral characteristics, in the range of rudder angles from  $-20^\circ$  to  $+20^\circ$ . Finer near-wall resolution is recommended for an accurate prediction of rudder side force at large rudder angle. At the magnitudes of rudder angle higher than  $20^\circ$ , the calculations tend to over-predict the extent of separation on the suction side of the rudder, which results in loss of accuracy in prediction of rudder forces. This result is connected with limitations of the isotropic turbulence model in use. The Moving Reference Frame method can be used as an approximation of time-accurate solution to predict averaged values of propeller and rudder characteristics, but its accuracy becomes lower for rudder forces at large rudder angles. The Mixing Plane method can not be recommended for use when the interaction between propeller and rudder is strong, e.g., due to heavy propeller loading and/or large rudder angle. At very low values of advance coefficient, convergence issues arise with the Mixing Plane method. The numerical Approach 2 employing unstructured polyhedral mesh and fine near-wall resolution is shown to adequately predict the extents of sheet cavitation on propeller blades and on rudder surface. It, however, remains a future task to implement a strict solution to the cavitation problem employing a multi-phase flow mixture model.

## REFERENCES

- Achkinadze, A. S., Berg, A., Krasilnikov, V. I. & Stepanov, I. E. (2003). 'Numerical Analysis of Podded and Steering Systems Using a Velocity Based Source Boundary Element Method with Modified Trailing Edge'. Proceedings of the Propellers/Shafting 2003 Symposium, Virginia Beach, VA, United States.
- Bensow, R. E., Huuva, T., Bark, G. & Liefvendahl, M. (2008). 'Large Eddy Simulation of Cavitating Propeller Flows'. Proceedings of the 27<sup>th</sup> Symposium on Naval Hydrodynamics, Seoul, Korea.
- Chang, P. A., Ebert, M., Young, Y. L., Liu, Zh., Mahesh, K., Jang, H. & Shearer M. (2008). 'Propeller Forces and Structural Response due to Crachback'. Proceedings of the 27<sup>th</sup> Symposium on Naval Hydrodynamics, Seoul, Korea.
- Han, K., Larsson, L. & Regnstrom, B. (2008). 'A Numerical Study of Hull/Propeller/Rudder Interaction'. Proceedings of the 27<sup>th</sup> Symposium on Naval Hydrodynamics, Seoul, Korea.
- Ghassemi, H. & Allievi, A. (1999). 'A Computational Method for the Analysis of Fluid Flow and Hydrodynamic Performance of Conventional and Podded Propulsion Systems'. Oceanic Engineering International 3(1).

- Jang, H. & Mahesh, K. (2008). 'Large Eddy Simulation of Ducted Propulsors in Crashback'. Proceedings of the 27<sup>th</sup> Symposium on Naval Hydrodynamics, Seoul, Korea.
- Kinnas, S., Natarajan, S., Lee, H., Kakar, K. & Gupta, A. (2003). 'Numerical Modelling of Podded Propulsors and Rudder Cavitation'. Proceedings of the Propellers/Shafting 2003 Symposium, Virginia Beach, VA, United States.
- Krasilnikov, V. I., Berg, A. & Øye, I. J. (2003). 'Numerical Prediction of Sheet Cavitation on Rudder And Podded Propellers Using Potential And Viscous Flow Solutions'. Proceedings of the 5<sup>th</sup> International Symposium on Cavitation CAV2003, Osaka, Japan.
- Krasilnikov, V. I. & Sun, J. (2008). 'Verification of an unsteady RANSE method for the analysis of marine propellers for high-speed crafts'. Proceedings of the International Conference SuperFAST'2008, St Petersburg, Russia.
- Krasilnikov, V. I., Sun, J., Zhang, Zh., & Hong, F. (2007). 'Mesh generation technique for the analysis of ducted propellers using a commercial RANSE solver and its application to scale effect study'. Proceedings of the 10<sup>th</sup> Numerical Towing Tank Symposium (NuTTS'07), Hamburg, Germany.
- Krasilnikov, V. I., Zhang, Zh., & Hong, F. (2009). 'Analysis of Unsteady Propeller Blade Forces by RANS'. Proceedings of the First International Symposium on Marine Propulsors SMP'09, Trondheim, Norway.
- Lübke, L.O. (2007). 'Investigation of a Semi-Balanced Rudder'. Proceedings of the 10<sup>th</sup> Numerical Towing Tank Symposium (NuTTS'07), Hamburg, Germany.
- Sánchez-Caja, A., Sipilä, T. P. & Pylkkänen, J. V. (2008). 'Simulation of the Incompressible Viscous Flow around Ducted Propellers with Rudders Using a RANSE Solver'. Proceedings of the 27<sup>th</sup> Symposium on Naval Hydrodynamics, Seoul, Korea.
- Sánchez-Caja, A., Sipilä, T. P. & Pylkkänen, J. V. (2009). 'Simulation of Viscous Flow around a Ducted Propeller with Rudder Using Different RANS-Based Approaches'. Proceedings of the First International Symposium on Marine Propulsors SMP'09, Trondheim, Norway.
- STAR-CCM+. (2009). STAR-CCM+ User Guide CD-Adapco, www.cd-adapco.com.

## APPENDIX A1

Comparison of propeller and rudder forces obtained by the Approach 1 and the Approach 2 using different solution methods at  $J=0.4$ ,  $\delta_R=-20^\circ$ .

	$K_{TP}$	$K_{QP}$	$K_{XR}$	$K_{XHB}$	$K_{XRTOT}$	$K_{YR}$	$K_{YHB}$	$K_{YRTOT}$
<b>Approach 1</b> <b>MRF</b> <b>OW</b>	0.4066	0.0641	-0.0603			0.1751		
<b>Approach 1</b> <b>MP</b> <b>OW</b>	0.4030	0.0635	-0.0585			0.1537		
<b>Approach 1</b> <b>MRF+SM</b> <b>OW</b>	0.3996	0.0648	-0.0474			0.1816		
<b>Approach 2</b> <b>MRF+SM</b> <b>Tunnel</b>	0.3992	0.0648	-0.0460	-0.0010	-0.0470	0.1951	0.0259	0.2210
<b>Approach 2</b> <b>SM</b> <b>Tunnel</b>	0.4006	0.0647	-0.0467	-0.0023	-0.0490	0.1978	0.0246	0.2224
<b>Experiment</b> <b>Tunnel</b>	0.4050	0.0644			-0.0451			0.2257

Legend: MRF – Moving Reference Frame, MP – Mixing Plane, SM – Sliding Mesh, MRF+SM – SM simulation with MRF results used as initial conditions, OW – Open Water simulation, Tunnel – simulation including tunnel walls and headbox;  $K_{TP}$  – propeller thrust coefficient,  $K_{QP}$  – propeller torque coefficient,  $K_{XR}$  – rudder axial force coefficient,  $K_{XHB}$  – coefficient of axial force acting on the headbox,  $K_{XRTOT}=K_{XR}+K_{XHB}$ ,  $K_{YR}$  – rudder side force coefficient,  $K_{YHB}$  – coefficient of side force acting on the headbox,  $K_{YRTOT}=K_{YR}+K_{YHB}$ ;  $K_{T,X,Y}=F_{T,X,Y}/(\rho n^2 D^4)$ ,  $K_Q=Q/(\rho n^2 D^5)$ .